Impact of vertical mixing parameterizations on internal gravity wave spectra in regional ocean models

Ritabrata Thakur[1], Brian K. Arbic[1], Dimitris Menemenlis[2], Kayhan Momeni[3],

Yulin Pan[4], W. R. Peltier[3], Joseph Skitka[1], Matthew H. Alford[5], Yuchen Ma[3]

[1]Department of Earth and Environmental Sciences, University of Michigan, Ann Arbor, MI, USA

[2]Jet Propulsion Laboratory, California Institute of Technology, Pasadena, CA, USA

[3]Department of Physics, University of Toronto, Toronto, Canada

[4]Department of Naval Architecture and Marine Engineering, University of Michigan, Ann Arbor, MI, USA

[5]Scripps Institution of Oceanography, University of California San Diego, La Jolla, CA, USA

Key Points:

- Regional ocean simulations are ideal for examining sensitivity of IGW spectra to model mixing parameters
- Turning off the KPP background yields more realistic IGW vertical structure in high-resolution regional models
- IGW spectra are most correctly estimated in models away from tidal generation sites and lateral boundaries

---

Corresponding author: Ritabrata Thakur, `ritabrata90official@gmail.com`

Abstract

We present improvements in the modeling of the vertical wavenumber spectrum of the internal gravity wave continuum in high-resolution regional ocean simulations. We focus on model sensitivities to mixing parameters and comparisons to McLane moored profiler observations in a Pacific region near the Hawaiian Ridge, which features strong semidiurnal tidal beams. In these simulations, the modeled continuum exhibits high sensitivity to the background mixing components of the K-Profile Parameterization (KPP) vertical mixing scheme. Without the KPP background mixing, stronger vertical gradients in velocity are sustained in the simulations and the modeled kinetic energy and shear spectral slopes are significantly closer to the observations. The improved representation of internal wave dynamics in these simulations makes them suitable for improving ocean mixing estimates and for the interpretation of satellite missions such as the Surface Water and Ocean Topography (SWOT) mission.

Keywords: internal gravity waves, vertical wavenumber spectra, MITgcm, KPP mixing parameterization

Plain Language Summary

Internal waves exist in the ocean interior due to differences in fluid densities. Breaking internal waves cause mixing, which has important effects on ocean temperatures and nutrients. Interactions between internal tides generated by tidal flow over bathymetric features and near-inertial waves generated by wind yield a spectrum of internal waves at many frequencies. Here, we compare the internal wave spectrum in high-resolution numerical simulations of a region in the North Pacific with observations from moored instruments. We study the effects of the background mixing components of the widely used K-Profile Parameterization (KPP) vertical mixing scheme on the vertical structure of the internal wave field. The KPP background parameterizes the mixing action of internal waves, which is not resolved in coarser-resolution global ocean models. In our high-resolution simulations, the internal wave field is highly active, and the KPP background components turn out to be mostly redundant in this setting. The modeled internal wave field lies closer to observations when we turn off the KPP background. Improved internal wave representation in ocean models can play an important role in the accurate representation of internal-wave-driven

mixing in ocean simulations and interpretation of internal wave signatures from the Surface Water and Ocean Topography mission.

1 Introduction

This paper focuses on the vertical structure of the internal gravity wave (IGW; also simply "internal wave", or IW) spectrum in regional ocean models. At tidal frequencies, IWs are called internal tides (ITs) and are primarily generated by large-scale barotropic tides moving over topography (e.g., Baines, 1982; Bell, 1975). High-frequency changes in wind forcing generate near-inertial (NI) IWs at the ocean surface, having frequencies close to the Coriolis frequency (reviewed in Alford et al. (2016)). The high-frequency IW continuum is thought to arise from nonlinear interactions of ITs, NI motions, and the IW continuum, and also due to local exchanges between ITs and low-frequency motions (e.g., van Haren, 2016; Barkan et al., 2017). The variable distribution of IWs and IW-generated turbulence (Kunze, 2017b) inspire continued interest due to its importance in vertical temperature redistribution (e.g., as in the Arctic; D'Asaro & Morison, 1992) and the global overturning circulation (Munk & Wunsch, 1998; Wunsch & Ferrari, 2004; Kunze, 2017a), their role in the enhancement of primary productivity by redistribution of nutrients (X. Pan et al., 2012), and important feedback to climate (MacKinnon et al., 2017; Whalen et al., 2020).

Global high-resolution ocean general circulation models with simultaneous tidal and atmospheric forcing carry a partially-resolved IW continuum (Müller et al., 2015; Rocha, Chereskin, et al., 2016; Arbic et al., 2018). These global models fall short of representing the real ocean due to a lack of resolution and/or insufficient parameterization of unresolved sub-grid scale physical processes such as IW breaking. Regional ocean models have been shown to display improved IW spectra over those in the global models when run at higher horizontal and vertical resolutions, as long as the lateral boundary forcing includes remotely-generated IWs from a global IW model (Mazloff et al., 2020; Nelson et al., 2020). Such remotely-forced regional models run over short periods are relatively affordable computationally and can be used to study the sensitivity of the IW continuum due to changes in model parameters.

Here, we study high-resolution regional simulations of the Massachusetts Institute of Technology general circulation model (MITgcm; Marshall et al., 1997) forced at their lateral boundaries by a global MITgcm simulation, named LLC4320, that has been widely studied (e.g., Rocha, Chereskin, et al., 2016; Rocha, Gille, et al., 2016; Savage et al., 2017; Su et

78 al., 2018). Regional simulations forced by LLC4320 have recently been used to study the

79 sensitivity of the IW continuum to model resolution (Nelson et al., 2020) and to under-

80 stand the mechanisms involved in the formation of the continuum (Y. Pan et al., 2020). In

81 this paper, we study the sensitivity of the IW vertical wavenumber spectra to the cumula-

82 tive effect of the background vertical viscosity and diffusivity components of the K-Profile

83 Parameterization (KPP; Large et al., 1994).

84 In our regional simulations, we focus on a region in the Pacific Ocean northward of

85 Hawaii (Fig 1). This region has heightened semi-diurnal (M_2) ITs that propagate northward

86 from the islands (Fig 1 (b)) and undergo parametric subharmonic instability (PSI) at the

87 critical latitude of 28.8° N, where the local inertial frequency is half of the M_2 tidal frequency.

88 In contrast with the shear field at other latitudes in this region, marginally-stable shear layers

89 with elevated NI energy generated via PSI of the IT are observed at 28.8° N (Alford et al.,

90 2007). The northward-propagating ITs also interact with southbound IT beams from the

91 Aleutian Ridge (not in the simulation domain), generating a complex IT field (e.g., Zhao

92 et al. (2010); Alford et al. (2019)). We present improvements in the modeled IW vertical

93 structure in these regional simulations by comparing them to observational data obtained

94 using McLane moored profilers (Doherty et al., 1999; Morrison et al., 2001) (Fig 1 (b)). We

95 find that the vertical wavenumber spectra of KE and shear shows appreciable improvement

96 when the KPP background mixing is turned off. We also discuss the characteristics of shear

97 spectra across different frequency bands in simulations with the KPP background turned off.

98 The model captures the vertical structure of the NI band, which is an important component

99 of the total shear, whereas the primary deficiency of the model relative to observations lies in

100 the high-frequency (supertidal) IW continuum. We further study the sensitivity of modeled

101 strain spectra to the KPP background components and quantify spectral improvements with

102 model vertical resolution.

2 Data and methods

2.1 MITgcm model

105 Using the MITgcm, we simulate a $6° \times 8°$ region north of the French Frigate Shoals,

106 Hawaii, in the Pacific Ocean as shown in Fig 1. We study a suite of regional ocean sim-

107 ulations with 109, 153, and 264 vertical levels and a constant horizontal grid spacing of

108 $1/48°$ (∼2km in the simulation domain). The vertical level thicknesses of our regional sim-
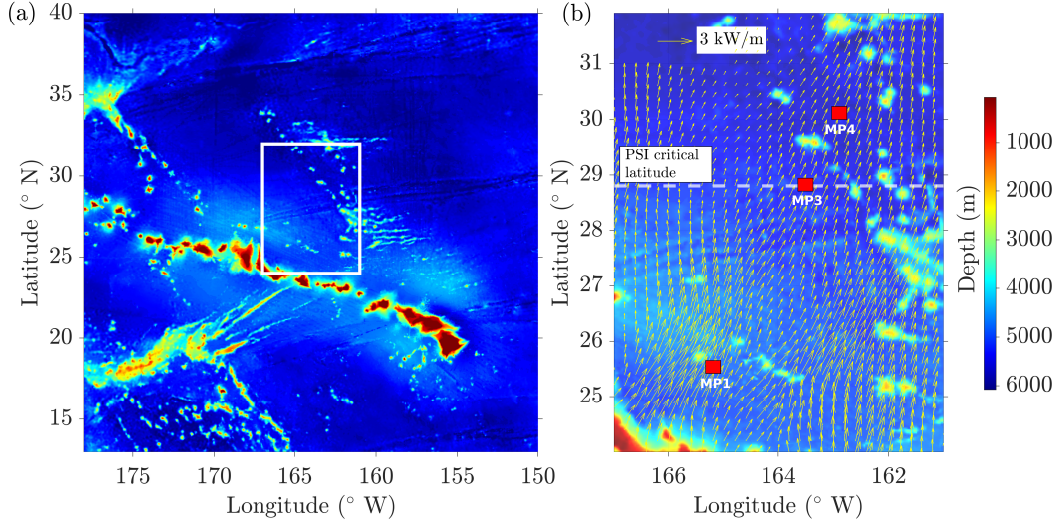
Figure 1. (a) The domain of study north of Hawaii is marked by the white rectangle. (b) An expanded view of the simulation domain. The locations of the McLane moored profilers (MP1, MP3, and MP4) are marked as red solid blocks. Yellow arrows show the energy flux of the mode-1 M_2 internal tide from satellite altimetry (Zhao et al., 2016; Zhao, 2022). The white dashed line at 28.8° N is the critical latitude for parametric subharmonic instability (PSI; e.g., MacKinnon et al., 2013). The model bathymetry from Smith and Sandwell (1997) is shown in color in each subplot.

ulations are identical to those of the LLC4320 simulation upto a certain depth but max out at thicknesses of Δz=100m below 2250m, Δz=50m below 1110m, and Δz=25m below 300m for the 109, 153, and 264-level simulations, respectively (see Fig S1). These regional simulations begin on 1 March 2012 and run for 73 days with initial fields taken from the global LLC4320 simulation, which employs the same grid spacing in the horizontal and 90 z-levels in the vertical direction (Rocha, Chereskin, et al., 2016; Savage et al., 2017). At the lateral boundaries, the regional simulations are forced by fields from the global LLC4320 simulation, which also includes remotely-generated IWs. All the simulations are forced with realistic atmospheric fields and astronomical tidal potential. Velocities, temperature, and salinity are stored at hourly intervals. (More in the SI.)

2.2 Observations

McLane moored profilers (MP) are deployed on oceanographic moorings and vertically profile the water column at 10–33 cm s^{-1} (Doherty et al., 1999). MPs record velocities, temperature, conductivity, pressure, and other oceanic variables in hourly intervals. We use

data from three MPs, deployed in the Pacific during the Internal Waves Across the Pacific experiment (Alford et al., 2007) along track 249 of TOPEX-Poseidon. The MP locations are marked as MP1 (194.8° E, 25.5° N), MP3 (196.5° E, 28.8° N), and MP4 (197.1° E, 30.1° N) in Fig 1 (b). The MP data are available in the depth range of 85–1384m with a vertical resolution of ∼2m, from 25 April–05 June 2006 at MP1 and MP3, and from 25 April–17 May 2006 at MP4.

2.3 Spectra calculations

Prior to vertical wavenumber spectra calculations with both model output and MP data, the horizontal velocities and the depths are WKBJ-scaled using local buoyancy frequency following Leaman and Sanford (1975) and interpolated to equally-spaced vertical coordinates (see Fig S2 and text in the SI). All vertical wavenumber spectra presented in this paper are averages of individual spectra over the model runtime and MP deployment periods, giving ∼1700 degrees of freedom (dof) for models and 530–950 dof for MPs assuming the spectra to be mutually independent. Velocities at the top and bottom of the depth range of spectra calculation are smoothly tapered to zero values using a Hanning window, and the lost variance due to this tapering is added back to the total variance. There is no segmenting of data in the vertical direction in our computations of spectra. (More in the SI.)

3 Model parameterizations

The interior vertical mixing parameterization scheme in the simulations is KPP (Large et al., 1994), and the horizontal mixing is governed by the Leith parameterization for 2D turbulence (Leith, 1968). The Leith scheme is modified with an added damping term for the divergent flow field (Fox-Kemper & Menemenlis, 2008). The effect of this modified Leith scheme on the modeled IW fields in high-resolution regional models is not considered here but will be discussed in future studies.

There are three controlling parameters which cumulatively act within the KPP scheme for the ocean interior mixing away from the upper mixed layer: (a) Richardson number-dependent shear-driven mixing, (b) a constant (in both space and time) background mixing to compensate for the breaking of unresolved IWs, set to 5.66×10^{-4} m^2s^{-1} as viscosity in the momentum equations and 5.44×10^{-7} m^2s^{-1} for temperature and salt diffusivity in LLC4320, and (c) double-diffusive mixing which is not implemented in any of the simulations

153 here. The KPP background has constant damping coefficients for energy dissipation that
154 act at all spatial locations, time steps, and vertical scales of the simulations. Also, if the fluid
155 column becomes convectively unstable, it undergoes immediate mixing in the simulations.

156 With an increase in vertical resolution, models better capture the small-scale density
157 and velocity fluctuations associated with an improved IW field. This raises the question of
158 whether the KPP background, which parameterizes IW-driven mixing in coarser-resolution
159 models that have reduced IW activity, would still be needed with an increase in model
160 resolution. In the following sections, we quantify the effect of KPP background on the
161 modeled spectra primarily using results from the highest-resolution (264-level) simulations
162 (with results from lower-resolution simulations summarized in the SI).

4 Spectral estimates and discussion

164 In the high-wavenumber regime, Cairns and Williams (1976)'s revision of the Garrett
165 and Munk (1972, 1975) spectrum—GM76—predicts a universal form of the kinetic energy
166 (KE) spectrum $E(m) \sim m^{-2}$, where m are the (stretched) vertical wavenumbers defined here
167 as the inverse of the stretched depths (also see the SI). The GM76 shear and strain spectra
168 derived from $E(m)$ have spectral slopes of m^0 at high-wavenumbers. However, extensive
169 high-resolution observations have demonstrated that these spectral slopes are variable in
170 different regions of the world's ocean (as reviewed in Polzin and Lvov (2011)). Pollmann
171 (2020) provides a global estimate of these spectral slopes and shows that the slopes deviate
172 significantly from that suggested by the empirical GM76 model. Therefore, in the following
173 discussions, we will consider the observed spectra as the "truth" in our comparison of the
174 modeled and observed spectra and include GM76 spectral slopes as reference.

4.1 Kinetic energy spectra

176 In our regional domain (Fig 1 (b)), vertical wavenumber spectra of KE from the ob-
177 servations differ from the GM76 slope of m^{-2} (Fig 2). At wavenumbers higher than 0.02
178 cpm (not shown), observed KE spectral slopes from the MPs are nearer to -2.4. Combined
179 with the frequency spectral slopes at these sites, this value is closer to the induced-diffusion-
180 dominated solutions predicted by wave turbulence theory (e.g., Lvov et al., 2010; Y. Pan et
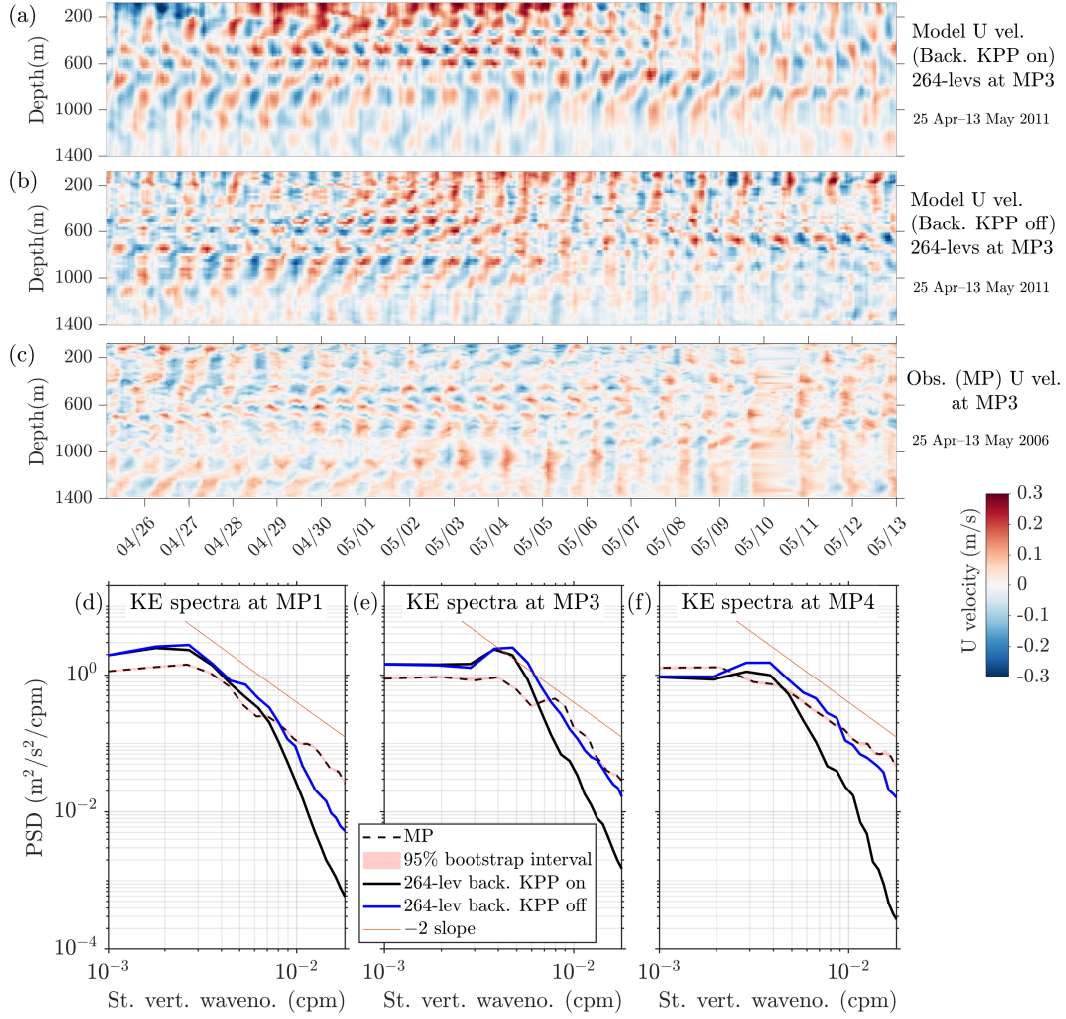181 al., 2020) than to the GM76 slope.

Figure 2. Time-depth plots of zonal (U) velocity from 264-level simulations at the MP3 location and over the depth range of 80–1400 m, with the KPP background (a) on and (b) off, are compared to observed zonal velocity in (c). The model output and the observations are from the same days of the year but different years. In (d–f), KE spectra in the same depth range for 264-level simulations (solid curves) at locations marked in Fig 1 (b) are compared to observed KE spectra (dashed curves) in the depth range of 85–1384m. The solid black curves are the modeled KE spectra with the KPP background on, while the blue curves are the modeled KE spectra with the KPP background components set to zero. 95% bootstrap confidence intervals on the means of the observed KE spectra are drawn in each as light red shading (for simulations, the 95% confidence intervals are smaller than the thickness of the curves). The GM76 spectral slope of −2 is drawn in each for reference. KE spectra are also shown in Figs S3, S4, and S5 in the SI.

We find that the modeled velocities and the KE spectra are sensitive to the KPP background (Fig 2). A comparison of zonal velocities from the 264-level simulations (Fig 2 (a,b)) with that from the observations (Fig 2 (c)) shows that the velocity field has more small-scale features when the KPP background diffusivity and viscosity are both set to zero (Fig 2 (b)). Although a perfect agreement between the velocity field from the simulations and the observations is not expected, energetic events, including those due to tidally-induced periodic flows, have sharper vertical gradients in the simulation without the KPP background (Fig 2 (b)) roughly similar to that seen in the observations (Fig 2 (c)), whereas these gradients are more diffused in the simulation where the KPP background is kept on and has the same values as that of the KPP background in global LLC4320 simulation (Fig 2 (a)).

The effect of turning the KPP background off on the IW field is seen in the comparison of the spectral slopes of the modeled KE spectra to that of the observed KE spectra (Fig 2 (d–f)). At low wavenumbers (<0.003 cpm), both observed and modeled KE spectra with and without KPP background roll off to a limiting slope value near zero. The observed and the modeled spectra disagree within a factor of two at wavenumbers <0.003 cpm at all three MP locations. This disagreement may be due to the differences in the overall oceanic mesoscale variability, tidal or near-inertial fields given that the observations and the model simulations are not contemporaneous. The modeled KE spectra with and without the KPP background diverges at wavenumbers higher than 0.004 cpm in both the cases, suggesting a vertical scale where the KPP background starts to become active in the simulations. This vertical scale has a small variability depending on the geographical location within the domain and the vertical resolution of the model (Fig S3) and is also different in different frequency bands (Fig S4). However, the general conclusion is that the high-wavenumber spectral slopes of the modeled KE spectra with the KPP background turned off lie significantly closer to the observed KE spectra from the MPs (Figs 2 (d–f) and S3).

The greatest improvement in the modeled KE spectra without the KPP background is seen at the MP4 location which is farthest from the generation site of the M_2 tidal beam. The variance at the highest wavenumber is ∼40 times higher at MP4 with the KPP background turned off (Fig 2 (f)). The magnitude of increase in spectral variance at MP1 and MP3 at the highest wavenumber without the KPP background are comparable to each other but less than that at MP4. At MP3, which is ∼500km from the M_2 IT generation site, the improved modeled IW continuum spectral levels are an order of magnitude higher when the KPP background is turned off (Fig 2 (e)), and the levels display a good agreement with the

observed KE spectrum. However, the improved modeled spectrum at MP1 is still relatively deficient in the IW continuum. As all the locations have similar vertical stratification, this difference in the spectral improvement and the disagreement between the modeled and the observed spectra could most likely be due to the degree of proximity to the IT generation site. With MP1 being nearer to the IT generation site (Fig 1 (b)), the nonlinear interactions giving rise to the IW continuum have insufficient time to develop, when compared to MP3 or MP4, giving rise to a weaker overall KE spectrum.

Spectral improvement with the KPP background turned off is also observed in the 109- and 153-level simulations (Fig S3) signifying that in both high (264-level) and moderate vertical resolution simulations (109- and 153-levels), the KPP background may have to be turned off to achieve a realistic IW continuum in regional models. We also note that turning off the KPP background improves the modeled IW continuum at all frequencies as the high-wavenumber spectral variances are higher in both the highpass (high-frequency or supertidal) and lowpass frequency bands around a cutoff of 11.5 hr as well as in the semidiurnal and near-inertial frequency bands (shown for 264-level in Fig S4). The lowpass band includes semidiurnal and diurnal tides, and near-inertial and subtidal flows, while the highpass band includes the supertidal IW continuum. We further observe that the high-wavenumber KE variance in the deeper ocean (1500–4000m) progressively increases with an increase in the model vertical resolution (Fig S5).

4.2 Shear and strain spectra

The vertical shear spectrum is defined as $\Phi(m) = (2\pi m)^2 E(m)$ (Gregg et al., 1993). In what follows, we first describe the shear characteristics of the regional domain using MP observations and then compare it to the shear spectra from the 264-level simulation with the KPP background turned off to understand the strengths and deficiencies of the modeled shear in different frequency bands.

The observed shear from MPs is dominated by slowly-varying (lowpass) flows with periods greater than 11.5 hr at all vertical scales (Fig 3 (a, c, e)). As expected, the NI band contributes significantly to the total shear. Alford et al. (2017) find that the shear layers at the PSI latitude (MP3) persist for $\mathcal{O}(25)$ days. In contrast, the shear layers persist for $\mathcal{O}(7)$ days at other MP locations. This is reflected in the NI shear spectrum at MP3 which has the highest variance among the three locations (Fig 3 (c) compared to (a, e)). The NI
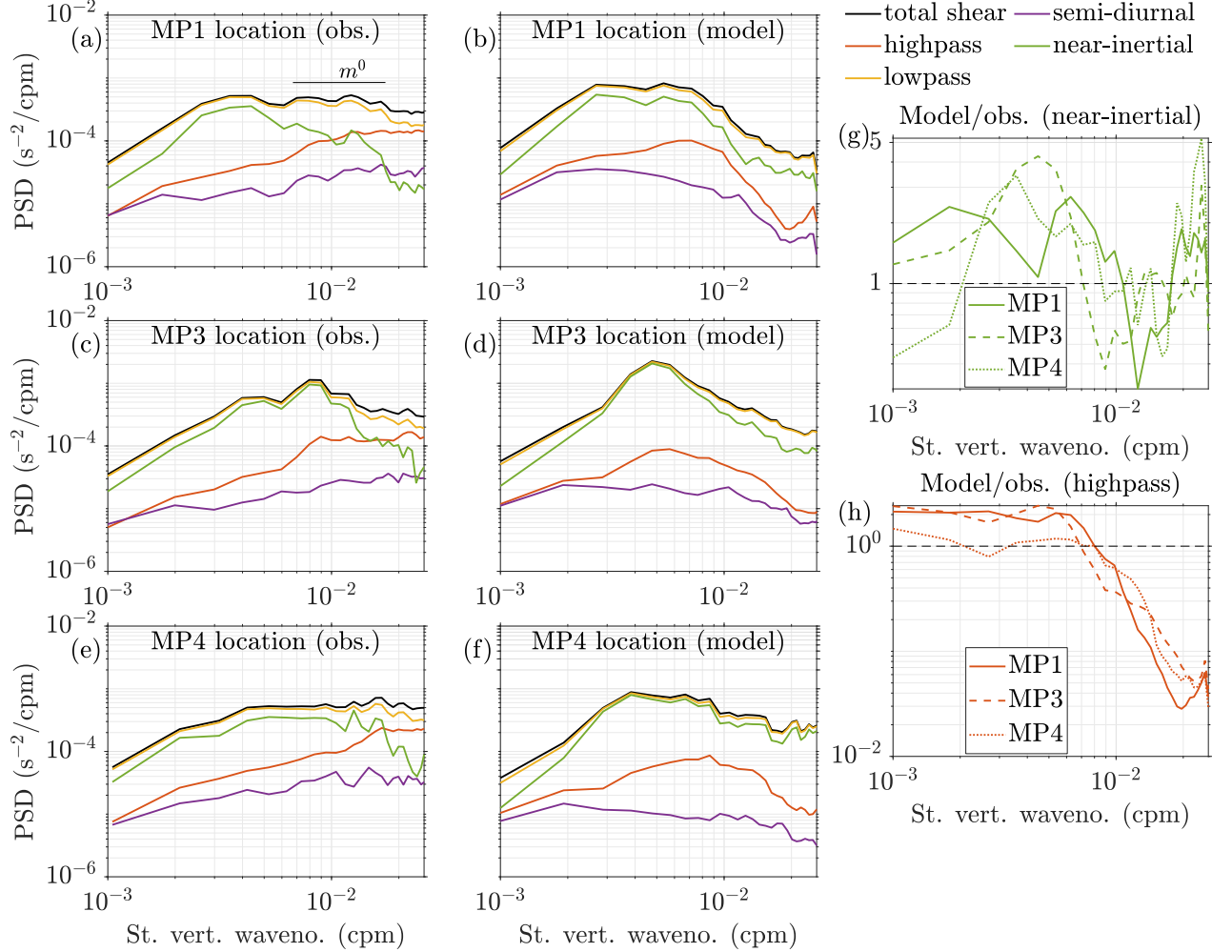
Figure 3. Shear spectra $\Phi(m)$ in different frequency bands from MP observations in (a), (c), and (e) are compared to modeled shear spectra from the 264-level simulation with the KPP background turned off in (b), (d), and (f). In each subplot, black is total shear, red is highpass or supertidal shear (>11.5 hr), yellow is lowpass shear (<11.5 hr), purple is semi-diurnal shear (11.5–13.5 hr), and green is NI shear (90–110% of the local inertial period). The high-wavenumber m^0 slope of the GM76 shear spectrum is denoted in (a). (g–h) The ratio of the modeled shear to observed shear, for the NI and highpass bands, respectively.

shear spectra have positive slopes up to 0.003 cpm at MP1 and $\sim$0.01 cpm at MP3 and MP4, after which they lose variances by an order of magnitude at MP1 and MP3. However, the NI shear at MP4 does not have much vertical variability and also has lower peak shear variance. The NI shear is geographically variable at small vertical scales in that it is a factor of 2–5 lower than the total shear at the highest wavenumber at MP3 and MP4 but approximately 20 times lower at MP1. The highpass shear is lower than the NI shear at low wavenumbers but has a higher variance than the NI shear above 0.01 cpm.

Similar to the observations, the modeled 264-level shear with the KPP background turned off is dominated by slowly-varying flows (Fig 3 (b, d, f)). The integrated modeled shear at the PSI latitude (MP3; Fig 3 (d)) is 1.2–2.5 times higher than at MP1 and MP4 (Fig 3 (b, f)) and attains the highest peak shear among the three locations. Considering the ratio of variance in the NI band (Fig 3 (g)), the modeled and the observed shear show reasonable agreement. In the highpass band, the model does not capture the transition as seen in the observed shear at 0.01 cpm as the modeled highpass shear remains lower than the respective modeled NI shear at all wavenumbers (e.g., comparing Fig 3 (a) and (b)). The ratio of the modeled to observed highpass shear (Fig 3 (h)) shows that in contrast to the other two locations, the modeled highpass shear at MP4 is within a factor of 1.5 of the observed highpass shear for a decade of wavenumbers from 10^{-3}–10^{-2} cpm. However, unlike the NI shear ratio, the modeled to observed highpass shear ratio decreases after 0.007–0.008 cpm and the modeled highpass shear is more than an order of magnitude less than the observations at the highest wavenumber (Fig 3 (h)). This reduction in high-wavenumber highpass shear variance could be attributed to the inability of the model to represent the cascade of energy to these vertical scales from low-frequency and NI motions due to a model grid spacing that is too coarse (see section 4 in the SI) or excessive damping by improper model parameterizations.

The modeled spectra of strain $(N^2 - \overline{N^2})/\overline{N^2}$, with N being the Brunt–Väisälä frequency and overbar denoting time mean, are lower in variance relative to the observed strain spectra (Fig 4 (a–c)). Except in the small range of 0.003–0.004 cpm at the MP1 location (Fig 4 (a)), the model is always lower than the observations in strain variance even in the highest resolution (264-level) simulations. Turning off the KPP background increases the strain variance by less than an order of magnitude at high wavenumbers, but this increase is not sufficient enough to bring the modeled strain variance up to the level of the observations. The largest increase in variance by turning off the KPP background is seen at MP4 (Fig 4

279   (c)), the location farthest from the IT generation site (Fig 1 (b)). Except in the NI band and

280   over a small range of wavenumbers, the modeled strain variance is an order of magnitude

281   too low over the majority of the wavenumbers in all frequency bands (Fig S6). In the deeper

282   ocean (below 1500m), an appreciable increase in the representation of modeled small-scale

283   strain is observed when the vertical resolution of the model is progressively increased (shown

284   for a small depth range of 1800–2200m in Fig 4 (d–f)). This improvement with an increase in

285   the model vertical resolution is reflected in the deep-ocean (1500–4000m) strain spectra (Fig

286   S7) which have the highest variance in the 264-level simulations. Improving the modeled

287   strain may involve refined temporal and spatial resolution as well as understanding the effect
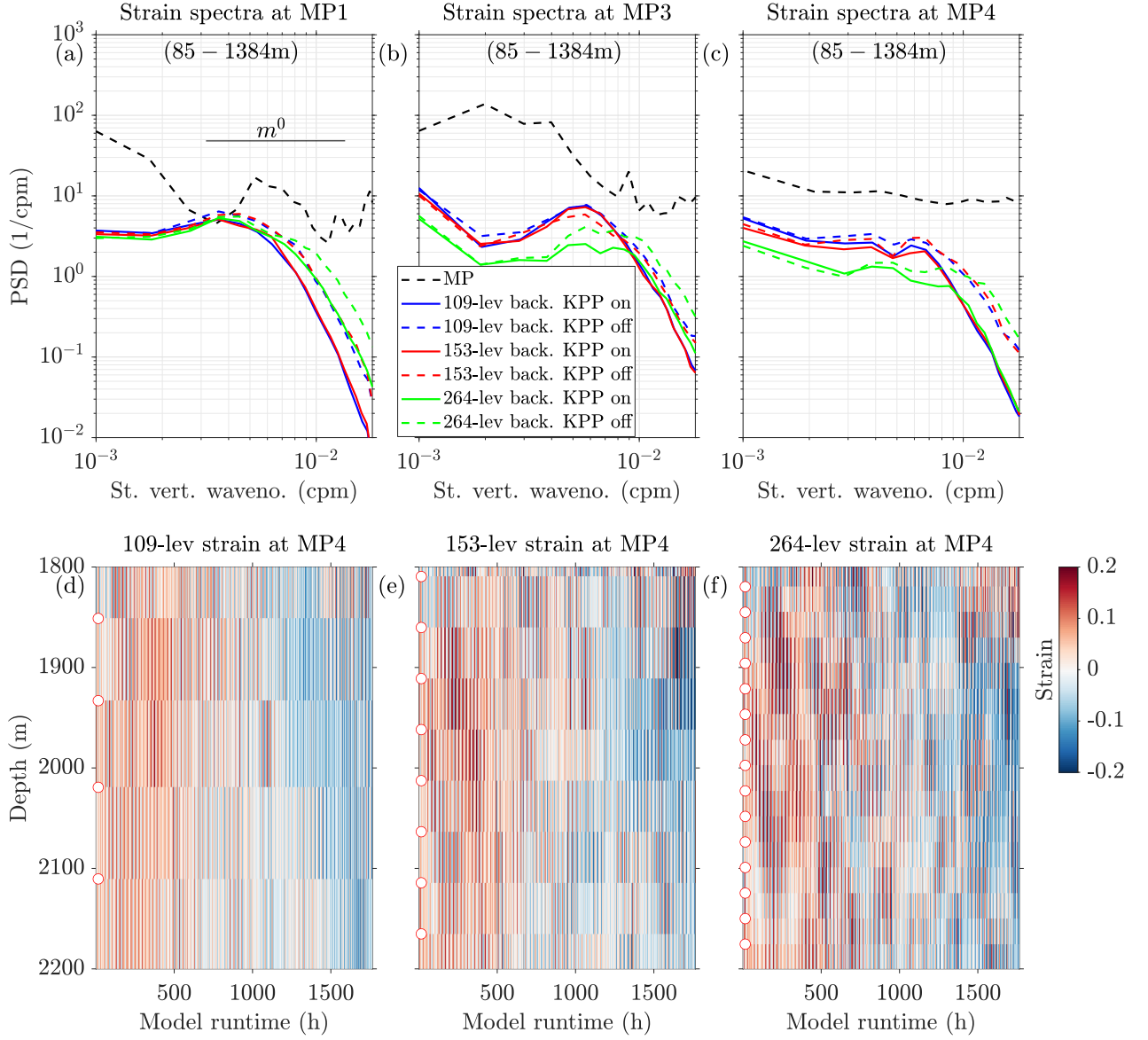
288   of other model parameterizations.

Figure 4. (a–c) Observed strain spectra (black dashed curves) for different locations in the depth range of 85–1384m are compared to modeled strain spectra from 109-, 153-, and 264-level simulations in the depth range of 80–1400m with and without the KPP background components. (d–f) Time-depth plots of the deeper ocean (1800–2200m) modeled strain at MP4 location without the KPP background components for three different vertical resolutions of the model. The filled circles on the y-axis are the locations of the model z-levels. The ratios of the modeled to observed strain in different frequency bands are in Fig S6 and the modeled strain spectra in the deep ocean (1500–4000m) are in Fig S7.

5 Conclusions

Regional simulations with higher vertical and horizontal resolutions can display improved IW spectra over those in the global simulations, as long as they are forced at their lateral boundaries by remotely-generated IWs from global simulations (Mazloff et al., 2020; Nelson et al., 2020). High vertical resolution regional simulations at the same horizontal grid spacing (∼2km) as the global LLC4320 are studied in this paper to explore the sensitivities of the modeled IW vertical structure to model parameterizations, in particular, the background mixing components of the K-Profile Parameterization (KPP; Large et al. (1994)). We show that the kinetic energy variance at the high vertical-wavenumber IW continuum increases and lies closer to the observations when the KPP background components are set to zero, with the agreement most notable in locations away from the tidal generation site of the Hawaiian islands. Thus, when high-resolution ocean models start resolving IWs, the KPP background, which compensates for breaking IWs in coarse-grid models that do not represent IW processes at all, should be turned down or even off to maintain the proper spectral level of the IW continuum.

The higher shear at the parametric subharmonic instability critical latitude is captured in the simulations with the KPP background turned off. The ability of the model to represent near-inertial shear, a critical component of the total IW shear, at all vertical wavenumbers is an encouraging start in understanding the space-time variability of IW shear using ocean models. However, the high-frequency or supertidal (>11.5 hr) component of the IW continuum shear is not adequately captured in this model. The simulations with the KPP background turned off are weaker in strain variance relative to the observed strain. The increase in modeled strain variance with the KPP background turned off is not enough to elevate the modeled spectral levels to that of the observations. This work can be developed in a few directions to address these model deficiencies and further improve the modeled IW continuum. We have not studied the sensitivity of the modeled spectra to the frequency of atmospheric forcing updates. We have also not explored the effects of increasing the horizontal resolution and the role of other model mixing parameterizations, most importantly, the Leith damping and the Richardson number-dependent shear-driven mixing component of the KPP and to what extent these govern mixing without the background components. These issues are likely to be important for accurate modeling of high-frequency shear and strain and will be discussed in future papers.

6 Open Research

The McLane moored profiler observations, regional MITgcm model simulation output, and the analysis codes used in this study are hosted at Harvard Dataverse at `https://doi.org/10.7910/DVN/HOVAPO`. The global LLC4320 simulation output is available at `https://data.nas.nasa.gov/ecco/`.

References

Adcroft, A., Campin, J.-M., Doddridge, S. D., Evangelinos, C., Ferreira, D., Follows, M., ... others (2018). Mitgcm documentation. *Release checkpoint67a-12-gbf23121*, *19*. Retrieved from `https://buildmedia.readthedocs.org/media/pdf/mitgcm/latest/mitgcm.pdf` (Accessed: 12-29-2021)

Alford, M. H., MacKinnon, J., Zhao, Z., Pinkel, R., Klymak, J., & Peacock, T. (2007). Internal waves across the Pacific. *Geophysical Research Letters*, *34*(24).

Alford, M. H., MacKinnon, J. A., Pinkel, R., & Klymak, J. M. (2017). Space–time scales of shear in the North Pacific. *Journal of Physical Oceanography*, *47*(10), 2455–2478.

Alford, M. H., MacKinnon, J. A., Simmons, H. L., & Nash, J. D. (2016). Near-inertial internal gravity waves in the ocean. *Annual Review of Marine Science*, *8*, 95–123.

Alford, M. H., Simmons, H. L., Marques, O. B., & Girton, J. B. (2019). Internal tide

352   attenuation in the North Pacific. *Geophysical Research Letters*, *46*(14), 8205–8213.

353   Arbic, B. K., Alford, M. H., Ansong, J. K., Buijsman, M. C., Ciotti, R. B., Farrar, J. T., . . .

354   others (2018). A primer on global internal tide and internal gravity wave continuum

355   modeling in HYCOM and MITgcm. In E. Chassignet, A. Pascual, J. Tintoré, &

356   J. Verron (Eds.), *New Frontiers in Operational Oceanography* (pp. 307–392). GODAE

357   OceanView.

358   Baines, P. G. (1982). On internal tide generation models. *Deep Sea Research Part A.*

359   *Oceanographic Research Papers*, *29*(3), 307–338.

360   Barkan, R., Winters, K. B., & McWilliams, J. C. (2017). Stimulated imbalance and the

361   enhancement of eddy kinetic energy dissipation by internal waves. *Journal of Physical*

362   *Oceanography*, *47*(1), 181–198.

363   Bell, T. (1975). Topographically generated internal waves in the open ocean. *Journal of*

364   *Geophysical Research*, *80*(3), 320–327.

365   Cairns, J. L., & Williams, G. O. (1976). Internal wave observations from a midwater float,

366   2. *Journal of Geophysical Research*, *81*(12), 1943–1950.

367   D'Asaro, E. A., & Morison, J. H. (1992). Internal waves and mixing in the Arctic Ocean.

368   *Deep Sea Research Part A. Oceanographic Research Papers*, *39*(2), S459–S484.

369   Doherty, K., Frye, D., Liberatore, S., & Toole, J. (1999). A moored profiling instrument.

370   *Journal of Atmospheric and Oceanic Technology*, *16*(11), 1816–1829.

371   Fox-Kemper, B., & Menemenlis, D. (2008). Can large eddy simulation techniques im-

372   prove mesoscale rich ocean models? *Washington DC American Geophysical Union*

373   *Geophysical Monograph Series*, *177*, 319–337.

374   Garrett, C., & Munk, W. (1972). Space-time scales of internal waves. *Geophysical Fluid*

375   *Dynamics*, *3*(3), 225–264.

376   Garrett, C., & Munk, W. (1975). Space-time scales of internal waves: A progress report.

377   *Journal of Geophysical Research*, *80*(3), 291–297.

378   Gregg, M., Winkel, D., & Sanford, T. (1993). Varieties of fully resolved spectra of vertical

379   shear. *Journal of Physical Oceanography*, *23*(1), 124–141.

380   Kunze, E. (2017a). The internal-wave-driven meridional overturning circulation. *Journal*

381   *of Physical Oceanography*, *47*(11), 2673–2689.

382   Kunze, E. (2017b). Internal-wave-driven mixing: Global geography and budgets. *Journal*

383   *of Physical Oceanography*, *47*(6), 1325–1345.

384   Large, W. G., McWilliams, J. C., & Doney, S. C. (1994). Oceanic vertical mixing: A review

and a model with a nonlocal boundary layer parameterization. *Reviews of Geophysics*, *32*(4), 363–403.

Large, W. G., & Yeager, S. G. (2004). *Diurnal to decadal global forcing for ocean and sea-ice models: The data sets and flux climatologies* (Tech. Rep.). University Corporation for Atmospheric Research. Retrieved from `http://dx.doi.org/10.5065/D6KK98Q6`

Leaman, K. D., & Sanford, T. B. (1975). Vertical energy propagation of inertial waves: A vector spectral analysis of velocity profiles. *Journal of Geophysical Research*, *80*(15), 1975–1978.

Leith, C. E. (1968). Diffusion approximation for two-dimensional turbulence. *The Physics of Fluids*, *11*(3), 671–672.

Losch, M., Menemenlis, D., Campin, J.-M., Heimbach, P., & Hill, C. (2010). On the formulation of sea-ice models. Part 1: Effects of different solver implementations and parameterizations. *Ocean Modelling*, *33*(1-2), 129–144.

Lvov, Y. V., Polzin, K. L., Tabak, E. G., & Yokoyama, N. (2010). Oceanic internal-wave field: Theory of scale-invariant spectra. *Journal of Physical Oceanography*, *40*(12), 2605–2623.

MacKinnon, J. A., Alford, M. H., Sun, O., Pinkel, R., Zhao, Z., & Klymak, J. (2013). Parametric subharmonic instability of the internal tide at 29 N. *Journal of Physical Oceanography*, *43*(1), 17–28.

MacKinnon, J. A., Zhao, Z., Whalen, C. B., Waterhouse, A. F., Trossman, D. S., Sun, O. M., ... others (2017). Climate process team on internal wave–driven ocean mixing. *Bulletin of the American Meteorological Society*, *98*(11), 2429–2454.

Marshall, J., Adcroft, A., Hill, C., Perelman, L., & Heisey, C. (1997). A finite-volume, incompressible Navier Stokes model for studies of the ocean on parallel computers. *Journal of Geophysical Research: Oceans*, *102*(C3), 5753–5766.

Mazloff, M. R., Cornuelle, B., Gille, S. T., & Wang, J. (2020). The importance of remote forcing for regional modeling of internal waves. *Journal of Geophysical Research: Oceans*, *125*(2), e2019JC015623.

Menemenlis, D., Campin, J.-M., Heimbach, P., Hill, C., Lee, T., Nguyen, A., ... Zhang, H. (2008). ECCO2: High resolution global ocean and sea ice data synthesis. *Mercator Ocean Quarterly Newsletter*, *31*(October), 13–21.

Morrison, A., Toole, J., Lukas, R., Worrilow, S., & Doherty, K. (2001). Results from the first successful field deployment of the McLane moored profiler. In *MTS/IEEE Oceans*

2001. An Ocean Odyssey. Conference Proceedings (IEEE Cat. No.01CH37295) (Vol. 2, p. 949-955).

Müller, M., Arbic, B. K., Richman, J. G., Shriver, J. F., Kunze, E. L., Scott, R. B., ... Zamudio, L. (2015). Toward an internal gravity wave spectrum in global ocean models. *Geophysical Research Letters*, *42*(9), 3474–3481.

Munk, W., & Wunsch, C. (1998). Abyssal recipes II: Energetics of tidal and wind mixing. *Deep Sea Research Part I: Oceanographic Research Papers*, *45*(12), 1977–2010.

Nelson, A., Arbic, B., Menemenlis, D., Peltier, W., Alford, M., Grisouard, N., & Klymak, J. (2020). Improved internal wave spectral continuum in a regional ocean model. *Journal of Geophysical Research: Oceans*, *125*(5), e2019JC015974.

Pan, X., Wong, G. T., Shiah, F.-K., & Ho, T.-Y. (2012). Enhancement of biological productivity by internal waves: observations in the summertime in the northern South China Sea. *Journal of Oceanography*, *68*(3), 427–437.

Pan, Y., Arbic, B. K., Nelson, A. D., Menemenlis, D., Peltier, W., Xu, W., & Li, Y. (2020). Numerical investigation of mechanisms underlying oceanic internal gravity wave power-law spectra. *Journal of Physical Oceanography*, *50*(9), 2713–2733.

Pollmann, F. (2020). Global characterization of the oceans internal wave spectrum. *Journal of Physical Oceanography*, *50*(7), 1871–1891.

Polzin, K. L., & Lvov, Y. V. (2011). Toward regional characterizations of the oceanic internal wavefield. *Reviews of Geophysics*, *49*(4).

Rocha, C. B., Chereskin, T. K., Gille, S. T., & Menemenlis, D. (2016). Mesoscale to submesoscale wavenumber spectra in Drake Passage. *Journal of Physical Oceanography*, *46*(2), 601–620.

Rocha, C. B., Gille, S. T., Chereskin, T. K., & Menemenlis, D. (2016). Seasonality of submesoscale dynamics in the Kuroshio Extension. *Geophysical Research Letters*, *43*(21), 11,30411,311.

Savage, A. C., Arbic, B. K., Alford, M. H., Ansong, J. K., Farrar, J. T., Menemenlis, D., ... others (2017). Spectral decomposition of internal gravity wave sea surface height in global models. *Journal of Geophysical Research: Oceans*, *122*(10), 7803–7821.

Smith, W. H., & Sandwell, D. T. (1997). Global sea floor topography from satellite altimetry and ship depth soundings. *Science*, *277*(5334), 1956–1962.

Su, Z., Wang, J., Klein, P., Thompson, A. F., & Menemenlis, D. (2018). Ocean submesoscales as a key component of the global heat budget. *Nature Communications*, *9*(1),

1–8.

van Haren, H. (2016). Do deep-ocean kinetic energy spectra represent deterministic or stochastic signals? *Journal of Geophysical Research: Oceans*, *121*(1), 240–251.

Welch, P. (1967). The use of fast Fourier transform for the estimation of power spectra: a method based on time averaging over short, modified periodograms. *IEEE Transactions on Audio and Electroacoustics*, *15*(2), 70–73.

Whalen, C. B., de Lavergne, C., Garabato, A. C. N., Klymak, J. M., Mackinnon, J. A., & Sheen, K. L. (2020). Internal wave-driven mixing: governing processes and consequences for climate. *Nature Reviews Earth & Environment*, *1*(11), 606–621.

Wunsch, C., & Ferrari, R. (2004). Vertical mixing, energy, and the general circulation of the oceans. *Annual Review of Fluid Mechanics*, *36*(1), 281–314.

Zhao, Z. (2022). Development of the yearly mode-1 M_2 internal tide model in 2019. *Journal of Atmospheric and Oceanic Technology*, *39*(4), 463–478.

Zhao, Z., Alford, M. H., Girton, J. B., Rainville, L., & Simmons, H. L. (2016). Global observations of open-ocean mode-1 M_2 internal tides. *Journal of Physical Oceanography*, *46*(6), 1657–1684.

Zhao, Z., Alford, M. H., MacKinnon, J. A., & Pinkel, R. (2010). Long-range propagation of the semidiurnal internal tide from the Hawaiian Ridge. *Journal of Physical Oceanography*, *40*(4), 713–736.